Front. Earth Sci. 2023, 17(1): 145–157
https://doi.org/10.1007/s11707-022-0980-7

RESEARCH ARTICLE

Adsorption and desorption behavior under coal–water–gas coupling conditions of high- and low-rank coal samples

Chen GUO[1,2,3], Jiang GOU[1], Dongmin MA (✉)[1,2,3], Yuan BAO[1,2,3], Qingmin SHI[1,2,3], Jiahao MENG[1], Junzhe GAO[1], Lingling LU[4]

1 College of Geology and Environment, Xi'an University of Science and Technology, Xi'an 710054, China
2 Shaanxi Provincial Key Laboratory of Geological Support for Coal Green Exploitation, Xi'an University of Science and Technology, Xi'an 710054, China
3 Geological Research Institute for Coal Green Mining, Xi'an University of Science and Technology, Xi'an 710054, China
4 Aerophoto Grammetry and Remote Sensing Bureau, China National Administration of Coal Geology, Xi'an 710100, China

Abstract High- and low-rank coalbed methane (CBM) are both important fields of CBM development in China, but their formation and production mechanisms differ considerably. The adsorption/desorption behavior of high- and low-rank coals under the coupling of coal–water–gas was investigated using two series of samples. Coal samples from Zhangjiamao (ZJM) coal mine, Ordos Basin, and Sihe (SH) coal mine, Qinshui Basin, were tested by isothermal adsorption–desorption experiment, natural imbibition experiment, nuclear magnetic resonance, mercury injection porosimetry, contact angle test, and permeability test. Isothermal adsorption and desorption experiments under dry, equilibrium water, and saturated water, were performed to explore the differences between the adsorption and desorption characteristics. The results show that the wettability and permeability of the ZJM low-rank coal sample was considerably higher than that of the SH high-rank coal sample. The imbibition process of the ZJM sample exhibited a high imbibition rate and high total-imbibition volume, whereas the SH sample exhibited a slow imbibition rate and low total-imbibition volume. The ZJM sample had a complex pore structure and diverse pore-size distribution with a lower mercury withdrawal efficiency at 59.60%, whereas the SH sample had a relatively uniform pore-size distribution with a higher mercury withdrawal efficiency at 97.62%. The response of adsorption and desorption of the ZJM sample to water was more significant than that of the SH sample. The desorption hysteresis of the ZJM sample was stronger than that of the SH sample and was more prominently affected by water, which was consistent with its strong wettability and complex pore-throat configuration. A comprehensive adsorption and desorption mode was constructed for high- and low-rank coal samples under coal–water–gas coupling condition. The research results are important to enrich the geological theory of high- and low-rank CBM and to guide efficient CBM recovery.

Keywords coalbed methane, adsorption–desorption, desorption hysteresis, wettability, pore structure, coal–water–gas coupling

Received October 31, 2021; accepted February 17, 2022

E-mail: makaay_@126.com

1 Introduction

Coal is a complex, multiple-pore medium with organic macromolecular structure as its skeleton. These pores are generally filled with gas and/or water, the coal–water–gas three-phase coupling effect controls the adsorption and desorption behavior of coalbed methane (CBM). Wettability is an important surface property of solid materials, which represents the affinity of a solid material surface to fluid (Alvarez and Schechter, 2016). For coal, wettability determines its water content and the spatial distribution of gas and water in pores and is a key factor in the coal–water–gas three-phase coupling system. CBM adsorption and desorption characteristics under the control of the wettability and water content of coal reservoirs have been reported in the several aspects: 1) the characteristic of coal wettability evolution and its main control factors (Arkhipov et al., 2014; Savitskyi, 2015; Ji et al., 2021; Wang et al., 2021); 2) the influence of surfactants on coal wettability and desorption rate (Abdulelah et al., 2021; Hu et al., 2021; Jia et al., 2021); 3) the influence of wettability and water content on adsorption/desorption capacity (Clarkson and Bustin, 2000; Qin et al., 2005; Sang et al., 2005; Azizian and Bashiri, 2008; Guo et al., 2017, 2021; Chen et al., 2021; Xu et al., 2021); 4) relationship between fluid type, wettability, and adsorption heat (Filippova, 1998; Madani et al., 2015; Grinev et al., 2016; Askalany

and Saha, 2017); and 5) the mass transfer mechanism during CBM desorption and production (Ma et al., 2018; Sun et al., 2018). The influences of coal petrographic properties on wettability and adsorption/desorption have also been discussed, indicating that organic matter abundance and vitrinite content are the significant factors (Oparin et al., 2014; Varma et al., 2015a, 2015b; Sharma et al., 2016; Mohanty et al., 2018).

There are considerable differences between high- and low-rank CBM in coal petrographic properties, pore structure, accumulation characteristics, and production mechanism, resulting in differences in exploration and exploitation methods (Shen et al., 2015; Li et al., 2017, 2020; Qin et al., 2018; Mohamed and Mehana, 2020; Salmachi et al., 2021). Understanding the difference in adsorption and desorption behavior under the constraints of wettability, porosity, and permeability can contributes to the determination of CBM distribution and enhancing recovery rate. This study considers the differences in physical properties between high- and low-rank coal samples and investigates their adsorption/desorption behaviors with different water content. By integrating the obtained experimental results, we attempt to construct a wettability-based adsorption–desorption model of high- and low-rank CBM. This work can provide a better understanding of the adsorption–desorption mechanism under the coal–water–gas three-phase coupling effect, as well as improve the geological understanding of CBM reservoir formation and development.

2 Samples and experiments

The samples were taken from coal seam No. 4^{-2} of the Yan'an Formation (J_{2y}), the Zhangjiamao (ZJM) coal mine in the Jurassic coalfield in northern Shaanxi, and coal seam No. 3 of the Shanxi formation (P_{1s}) of Carboniferous–Permian coal-bearing strata in the Sihe (SH) coal mine, southern Qinshui Basin. The coal samples were collected from the working face of coal mines by the grooving method and were wrapped with polyethylene film and transported to the laboratory for processing. Maceral analysis, proximate analysis, and physical property tests were performed on the coal samples. Particularly, the physical property tests included isothermal adsorption–desorption experiment (IADE), natural imbibition experiment (NIE), nuclear magnetic resonance (NMR), mercury injection porosimetry (MIP), contact angle (CA) test, and permeability test.

Cylindrical samples with a diameter of 25 mm were prepared from the raw coals along the laminae and were polished to conduct the IADE, NMR, NIE, MIP, CA, and permeability tests. The remaining samples were crushed to four levels of particle size as follows: 4–7 mesh (2.80–4.75 mm), 20–60 mesh (0.25–0.83 mm), 60–80 mesh (0.18–0.25 mm), and > 200 mesh (< 0.075 mm), which were used for MIP, maceral analysis, IADE, and proximate analysis, respectively (Fig. 1).

2.1 Maceral and proximate analysis

The maceral analysis and maximum vitrinite reflectance (%, $R_{o,max}$) tests were conducted according to ISO 7404-3 (2009) and ASTM Standard D2798-05. The proximate analysis was according to ASTM standard D3172-13.

2.2 MIP

This was performed on a Micromeritics AutoPore IV 9500 V1.09 mercury injection apparatus, according to the

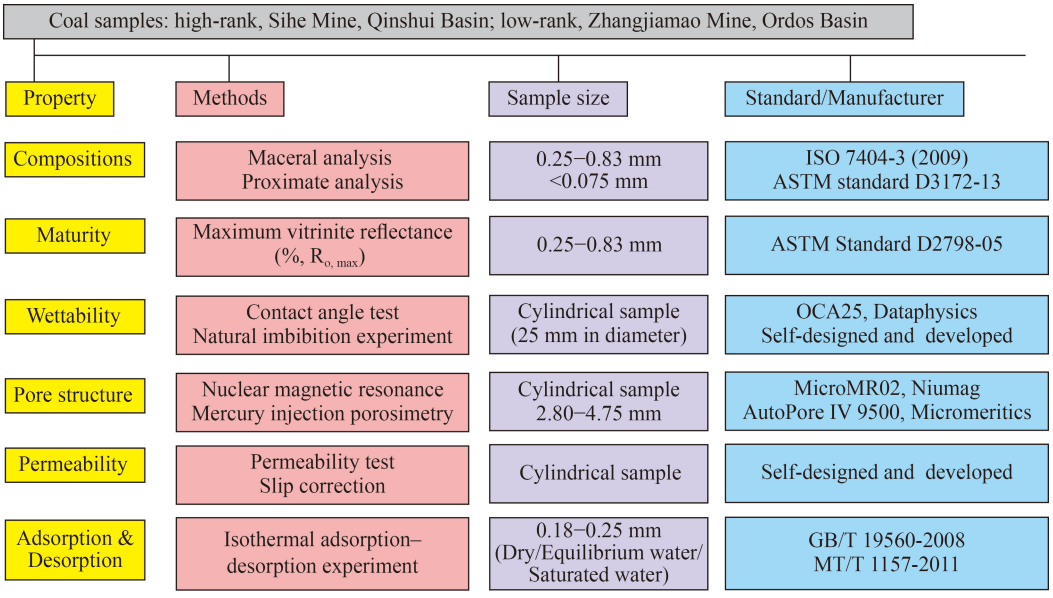

Fig. 1 Diagram of experimental scheme.

China standard SY/T 5346-2005. The lower limit of the testable pore size was 3.0 nm. The specific experimental method and principle of MIP were introduced in our previous studies (Guo et al., 2020a, 2020b).

2.3 IADE

This was performed on coal samples with three water-bearing states: dry, equilibrium water, and saturated water, based on the China standard GB/T 19560-2008. The experimental gas was high-purity methane (methane concentration 99.99%), the experimental temperature was 30°C, and the experimental pressure ranged from 0 to 11 MPa, with an equilibrium pressure interval of 1.5–2 MPa. The dry sample was prepared by drying the air-dried base sample in an oven at 100°C for 48 h. The equilibrium water sample was prepared according to the China standard MT/T 1157-2011. The saturated water sample was saturated via evacuation for 24 h and pressurization (15 MPa) for another 24 h.

2.4 CA

This was measured on an OCA25 video optical contact angle measuring instrument produced by Dataphysics, Germany, with CA measurements of 0–180°, an accuracy of ±0.1°, and a resolution of ±0.01°. Syringes were filled with deionized water and installed on the instrument injection unit. The volume of liquid droplets was set at 3 μL for each injection at an injection rate at 1 μL/s. Each sample was tested three times, and the average was taken as the final result.

2.5 NIE

The coal samples were placed in a measuring cylinder entirely submerged in distilled water with a water column height of 20 cm. The NIE was conducted under normal atmospheric pressure, and the water volumes of the coal after 1, 8, 20, 32, 52 h, and 100 h were recorded via a weighing method. Finally, the samples were saturated via evacuation for 24 h and pressurization (15 MPa) for another 24 h to achieve a fully saturated state. The water volumes of the saturated coal were recorded. NMR was performed on coal samples with different NIE time intervals and the saturated samples to obtain transverse relaxation time T_2 spectra and to better understand the evolutionary characteristics of the natural imbibition process and pore types of the coal samples.

2.6 Permeability test

The gas used for permeability tests was nitrogen (purity 99.99%) with a viscosity of 0.017805 mPa·s (25°C, 0.1 MPa). The samples were dried at 100°C for 24 h and placed in a permeability tester gripper. The gas permeability was measured at five set inlet pressure points while keeping the effective stress (1 MPa) and outlet pressure (0.1 MPa) constant. Finally, slip-effect corrections, based on the relation between the average gas pressure (P_m) and measured permeability, were performed to obtain the absolute permeability (equivalent liquid-phase permeability). The specific test method and principle of absolute permeability was given in our previous study (Guo et al., 2021).

3 Results

3.1 Maceral composition, coal quality, and contact angle

The maximum vitrinite reflectance (%, $R_{o,max}$) showed that SH sample was anthracite (high-rank coal) and ZJM sample was high-volatile bituminous coal (low-rank coal). The inertinite content of the ZJM sample was considerably higher than that of the SH sample, which is one of the characteristics of the Jurassic coal seam in northwest China. In addition, the mineral content of the ZJM sample was lower and the mineral type was mainly silica, whereas the SH sample was dominated by clay minerals. The proximate analysis results showed that the ZJM sample had a higher water content and volatile matter yield, belonging to high-volatile coal and ultralow ash coal; SH sample had a higher ash yield and fixed carbon content, belonging to ultralow-volatile coal and low-ash coal (Table 1).

The average CA of the ZJM sample was 61.18°, whereas that of the SH sample was 92.40°. The wettability of the ZJM sample was obviously better than that of the SH sample (Table 2; Fig. 2). The water wettability of coal is a characterization of the binding force between water and the coal surface. Specifically, it is mainly the hydrogen bonding force between water molecules and the polar functional groups of coal macromolecules. The

Table 1 Results of the maceral and proximate analysis

Sample	Coal seam	$R_{o,max}$/%	V/%	I/%	E/%	M/%	M_{ad}/%	A_d/%	V_{daf}/%	FC_{ad}/%
ZJM (J_{2y})	4^{-2}	0.61	55.90	43.20	0.50	0.50	3.40	6.47	44.75	49.92
SH (P_{1s})	3	3.04	88.12	8.75	0.00	3.13	1.09	11.37	8.02	80.64

Notes:V-Vitrinite, I-Inertinite, E-Exinite, M-Mineral, M_{ad}-Moisture content at air-dried basis, A_d-Ash yield at dry basis, V_{daf}-Volatile matter yield at dry ash-free basis, FC_{ad}-Fixed carbon content at air-dried basis, $R_{o,max}$-Maximum vitrinite reflectance in oil immersion.

Table 2 Results of the CA tests

Sample	Experiment number	CA/(°)	Error/(°)	Injection volume/μL	Average CA/(°)
ZJM	1	57.92	3.96	0.37	
	2	66.02	1.04	0.45	61.18
	3	59.61	2.79	0.39	
SH	1	99.30	1.58	0.43	
	2	88.35	2.27	0.43	92.40
	3	89.50	1.64	0.33	

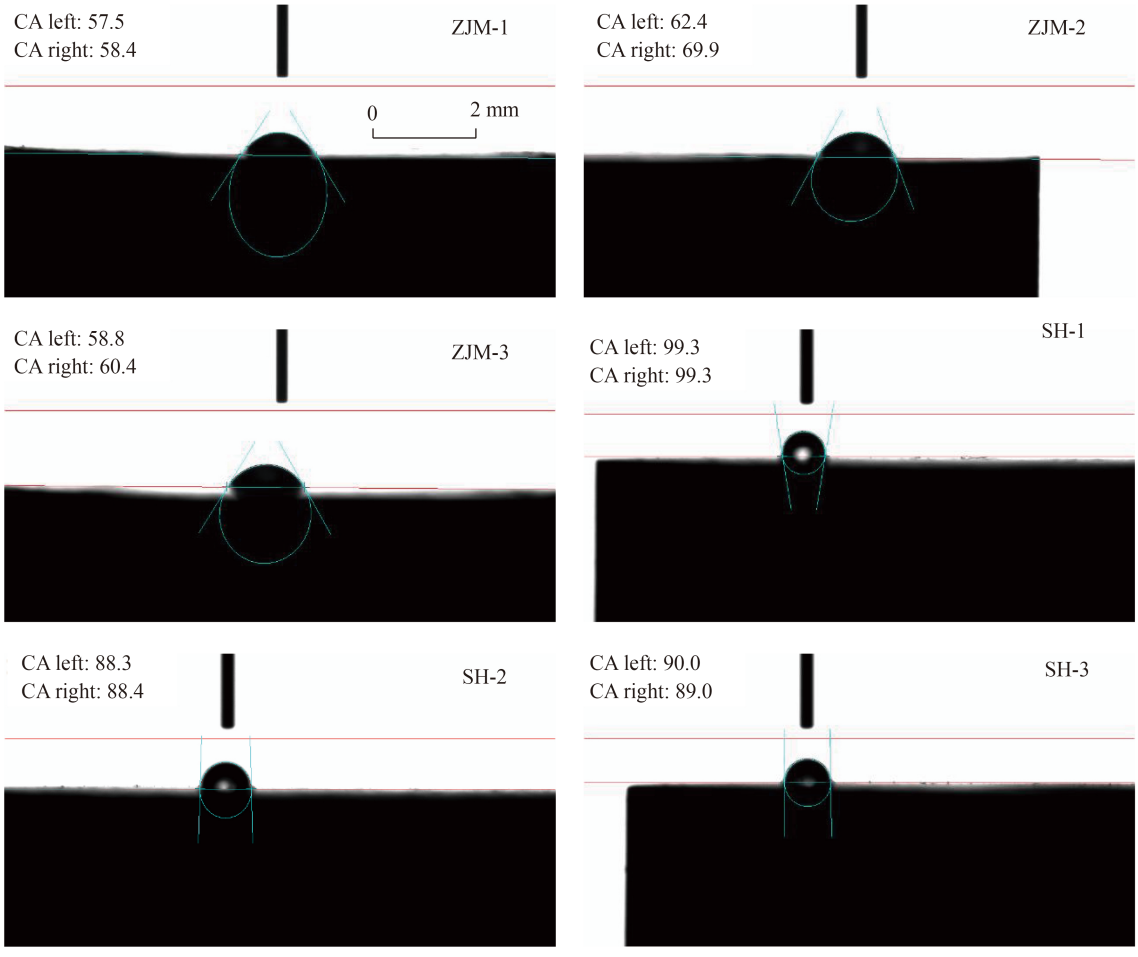

Fig. 2 Images of contact angle tests.

functional groups that experience a hydrogen-bonding force with water molecules mainly include carboxyl (–COOH), hydroxyl (–OH), and methoxy ($–OCH_3$) groups (Li and Li, 2016). The hydrogen-bonding force between carboxyl groups and water molecules is the strongest, which is the most important factor affecting the wettability of a coal surface, followed by hydroxyl groups (Zhang and Wu, 2017). High-volatile bituminous coal molecules contain more polar oxygen-containing functional groups than anthracite, particularly carboxyl and hydroxyl groups. The poor wettability of anthracite to water provides favorable conditions for the adsorption of methane on the pore surface of coal under the condition of coal–water–gas three-phase coexistence.

3.2 NIE and NMR

The volume of water invading the coal samples at different NIE time intervals is shown in Table 3, and the changes in water-based porosity and saturation at different time intervals were calculated, as shown in Table 4. Combined with NMR, the influence that invading water has on the pore structure of the coal samples can be better understood.

Table 3 Sample parameters and data recording of NIE and saturation

Sample	Diameter /mm	Length /mm	Volume /cm^3	Dry weight/g	1 h-wet weight/g	8 h-wet weight/g
SH	25.78	60.54	31.60	47.64	48.14	48.71
ZJM	25.81	37.83	19.79	23.18	25.54	25.67
Sample	20 h-wet weight/g	32 h-wet weight/g	52 h-wet weight/g	100 h-wet weight/g	Saturated wet weight/g	
SH	49.22	49.50	49.64	49.70	49.83	
ZJM	25.67	25.72	25.74	25.77	25.85	

Table 4 Changes in porosity and saturation at different stages of NIE and saturation

Sample	Porosity/%						
	1 h	8 h	20 h	32 h	52 h	100 h	Saturated
SH	1.58	3.39	5.00	5.89	6.33	6.52	6.93
ZJM	11.92	12.58	12.58	12.83	12.93	13.09	13.49
Sample	Saturation/%						
	1 h	8 h	20 h	32 h	52 h	100 h	Saturated
SH	22.83	48.86	72.15	84.93	91.32	94.06	100.00
ZJM	88.39	93.26	93.26	95.13	95.88	97.00	100.00

Figure 3 shows that the NIE process of the sample was considerably significantly different from that of the SH sample. The water intrusion rate of the sample was considerably higher than that of the SH sample. The ZJM sample absorbed most of the saturated water within 1 h, and the saturation was over 80%; SH absorbed water more gradually, showing the characteristics of a gradual increase in water content with the continuation of NIE time interval. The NIE results were consistent with the differences in wettability between high- and low-rank coal samples, as the imbibition rate of low-rank coal with a strong wettability is higher. In addition, the saturated water porosity of the ZJM sample was approximately twice that of the SH sample, which provided favorable conditions for water imbibition. In general, the NIE results of the ZJM sample showed the characteristics of rapid imbibition and a large total imbibition volume, whereas the SH sample showed the characteristics of slow imbibition and a small total imbibition volume.

The NMR curves at different imbibition time intervals of the ZJM sample presented multipeak characteristics, indicating a multiple-pore-structure system (Fig. 4(a)); The SH sample has single-peak characteristics with dominant left peak, indicating that pores are predominantly small pores (Fig. 4(b)). The multiple pore system of the ZJM sample provided favorable conditions for the rapid imbibition of water into the coal sample. The NMR response of the saturated water state featured a considerable increase in the left peak, indicating that the water increment in the saturated water state of the low-rank coal mainly originated from small pores (Fig. 4(a)). The left T_2 peak of the SH sample showed the characteristics of step-by-step imbibition (Fig. 4(b)).

Three types of pores were identified based on the T_2

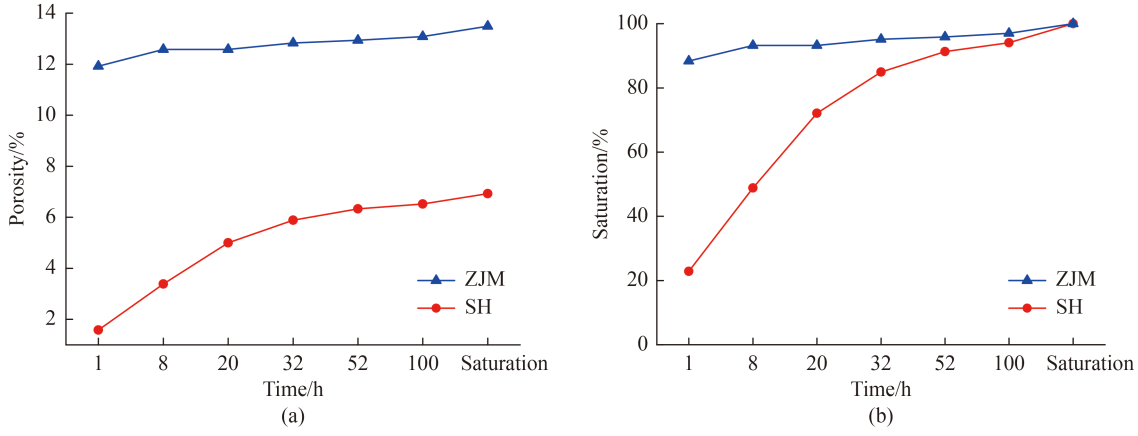

Fig. 3 NIE porosity and saturation evolution of coal samples.

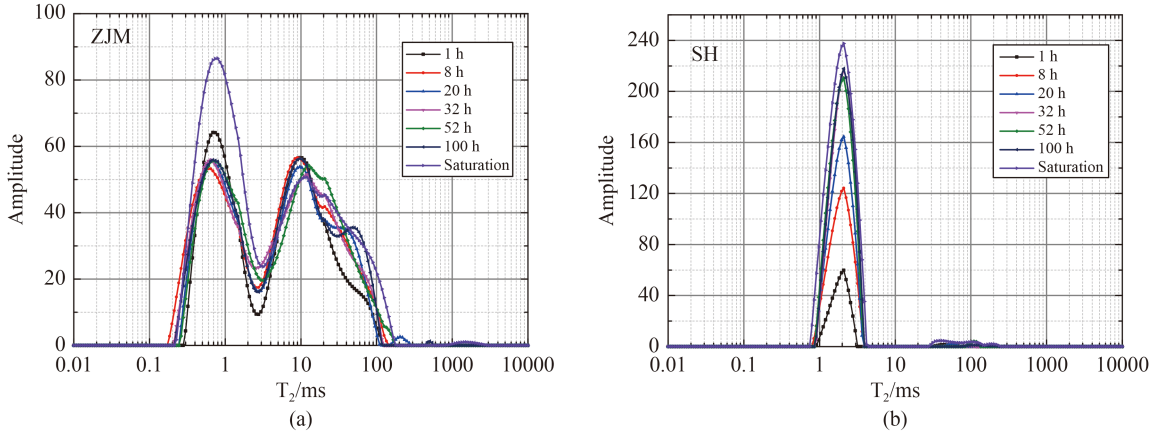

Fig. 4 NMR T_2 spectra of coal samples after NIE and saturation.

spectra, including mesopores (including micropores), macropores, and fractures (Yao and Liu, 2012). However, the T_2 thresholds distinguishing the three pore types varied between the different coal samples. In our study, T_2 values of 3 and 4 ms were selected to identify the mesopores and macropores for the ZJM sample and SH sample, respectively, and 100 ms was set to identify macropores and fractures for both ZJM and SH samples.

The variation in pore type during the NIE of the ZJM samples was not obvious, and the proportion of macropores was always higher than that of mesopores. The water content in the macropores slightly increased with the prolongation of imbibition time interval, whereas the water in the mesopores remained relatively stable. However, the amount of water invading the mesopores had increased in the saturated state, indicating that the water mainly invaded the mesopores in the saturated state. The proportion of mesopores was higher than that of macropores in the saturated state, differing from the NIE results (Fig. 5(a)).

During the NIE process of the SH sample, the water volume increased gradually and was dominated by the increase in mesopores. With continuing imbibition, the rate of increase tended to slow down. All pore types reached a maximal porosity under the saturated water state, where the most obvious increase was exhibited by macropores (Fig. 5(b)). The proportion of mesopores was considerably higher than that of macropores both in the NIE and saturated states for the SH sample.

After the rapid imbibition of macropores occurred in ZJM sample, the mesopores and micropores were easy to be blocked by water in the macropores, yielding no obvious change in water content in mesopores during the NIE process; The SH sample was characterized by a continual increase in mesopore water, indicating that no obvious blocking effect occurred. The water content under the saturated condition increased for both samples, reflecting that more pores were invaded by water in the pressurized saturation state. Particularly, the mesopore water increment was mainly because of the imbibition of mesopores that were blocked by macropore water during the NIE, as seen for the ZJM sample; the macropore and

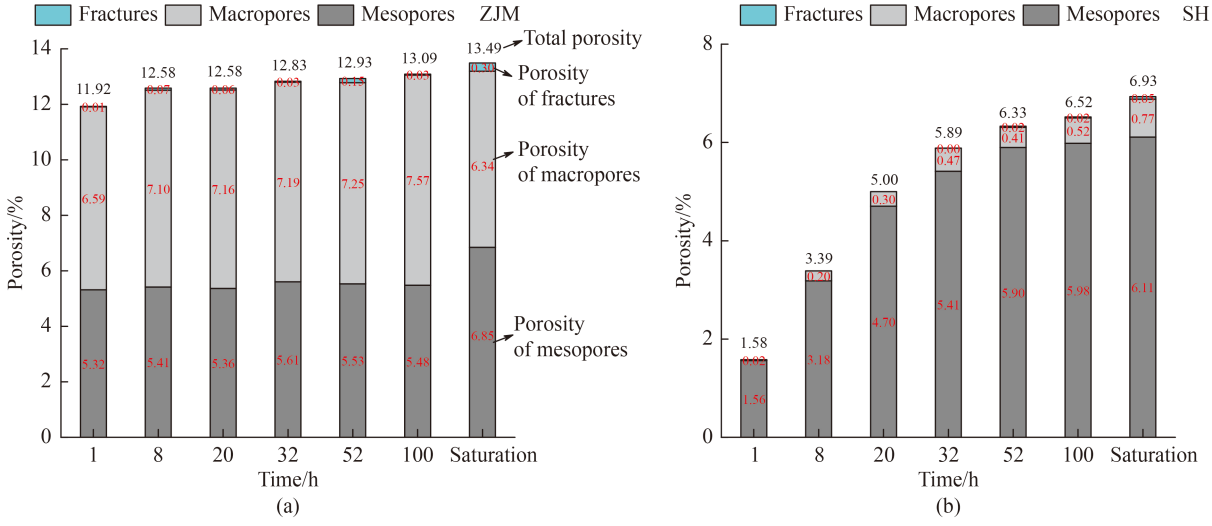

Fig. 5 Evolution of imbibition pore types of coal samples.

fracture water increment mainly originated from newly formed fractures during pressurized saturation, as seen for the SH sample.

3.3 Absolute permeability and pore structure

The absolute permeability of the SH sample was 0.0061 mD and that of the ZJM sample was 0.1154 mD (Fig. 6). The permeability of the ZJM sample was considerably higher than that of the SH sample. The saturated water porosity of the ZJM sample was almost twice that of the SH sample, and the permeability of the ZJM sample was two orders magnitude higher than that of the SH sample. This difference was further supported by MIP.

The pore structure parameters and mercury intrusion/extrusion curves obtained via MIP are shown in Table 5 and Fig. 7, respectively. The pore volume, specific surface area, pore size, and porosity of the ZJM sample were all higher than those of the SH sample.

From Fig. 7, the cumulative mercury intrusion volume of the ZJM sample was higher, with a lower mercury withdrawal efficiency (MWE) at 59.60%. The MWE of the SH sample was 97.62%. The MWE reflects the configuration relationship and homogenization degree of pores and throats. The higher the MWE, the more uniform the size of pores and throats. The low MWE of the ZJM sample showed that the configuration of pores and throats was complex, with a highly variable pore size. The high MWE of the SH sample showed a high homogenization degree of its pore-throat system. Figure 8 shows that the range of pore size distribution of the ZJM sample was wide, whereas that of the SH sample was concentrated at a pore size of <100 nm (Table 6). The pore structure of high-rank coal tends to homogenize toward a small pore size, which is consistent with the fact that the macromolecular structure of coal tends to be orderly and dense with continued coalification (Jin et al., 2017; Guo et al., 2018). The pore size of the ZJM sample was more diverse, and the pore structure was more complex than SH sample.

3.4 Adsorption and desorption

The water content of the coal samples in equilibrium water and saturated water states is shown in Table 7. The water content of the ZJM sample was higher than that of the SH sample both in the equilibrium and saturated water states, which was consistent with the differences in wettability of low- and high-rank coals.

The IADE data were fitted using the Langmuir equation to obtain isothermal adsorption/desorption curves and Langmuir constants. The Langmuir equation was established based on the equilibrium principle of gasification and coagulation kinetics. The adsorption pattern of gas on coal can be perfectly fitted by this model. The Langmuir adsorption isothermal equation is shown below:

$$V = \frac{V_L p}{p + P_L}, \tag{1}$$

where V is the adsorption volume, cm^3/g; p is the equilibrium pressure, MPa; V_L is the Langmuir volume, cm^3/g, representing the maximum adsorption capacity; P_L is the Langmuir pressure, MPa, representing the equilibrium pressure when the adsorption volume reaches half of V_L. V_L and P_L are known as the Langmuir constants.

The experimental results showed that the adsorption capacity gradually decreased moving from the dry,

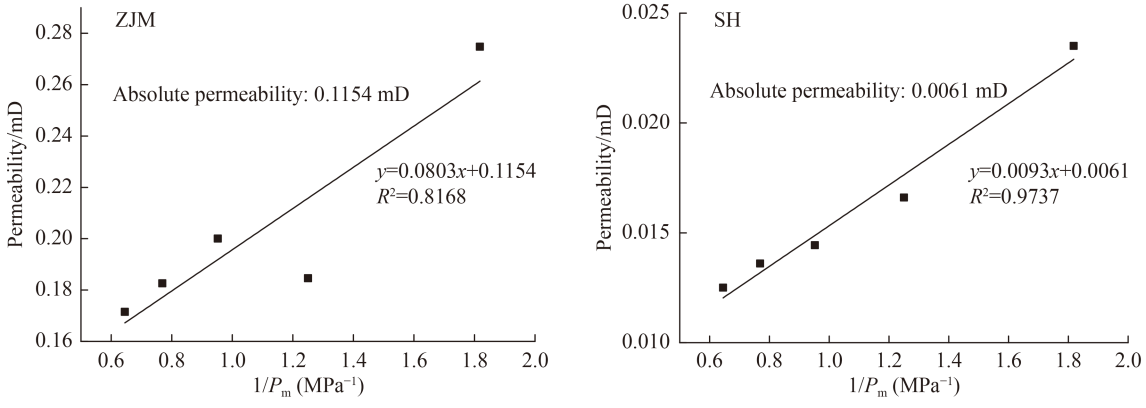

Fig. 6 Slip correction of coal sample permeability.

Table 5 Pore structure parameters of coal samples obtained from MIP

Sample	Pore volume /(cm^3·g^{-1})	Specific surface area/(m^2·g^{-1})	Volumetric median pore size/nm	Specific surface area median pore size/nm	Average pore size/nm	Porosity /%	Mercury withdrawal efficiency/%
ZJM	0.0917	40.939	11.65	4.90	8.96	9.74	59.60
SH	0.0262	18.151	6.63	4.10	5.77	3.13	97.62

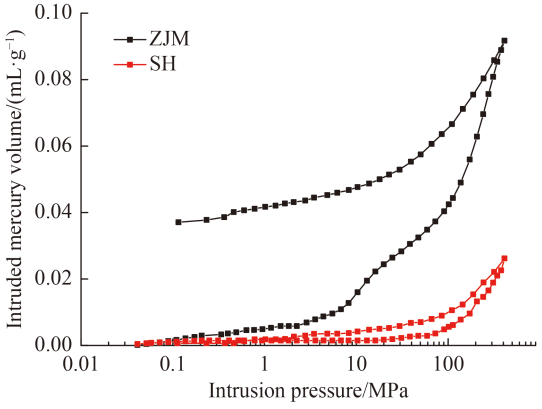

Fig. 7 Mercury intrusion and extrusion curves of coal samples.

equilibrium water, and saturated water states, and the SH sample had a higher adsorption capacity than the ZJM sample. The equilibrium water state of the ZJM sample had a large decrease in adsorption volume compared to the dry state, which was consistent with its strong wettability. The desorption curve of the saturated water state of the ZJM sample was obviously different from that of the other states, indicating that there was an obvious occurrence of the desorption hysteresis phenomenon (Fig. 9(a)). Water is crucial in the adsorption and desorption processes because it reduces the adsorption capacity of coal toward methane and hinders the efficient desorption of methane. The low correlation coefficient (R^2) of the fitted curve of desorption data under saturated water state also proved the strong hindering effect of water on desorption.

The adsorption/desorption curves of the SH sample under different water content states showed obvious differences. From the dry state to the saturated water state, the adsorption capacity gradually decreased with the increase in water content, indicating that water reduced the adsorption capacity. The desorption hysteresis of the equilibrium water state and saturated water state was stronger than that of the dry state, indicating the water hindered the desorption of CBM (Fig. 9(b)). The effect of water on the adsorption and desorption of the ZJM sample toward methane was considerably stronger than that of the SH sample, which was consistent with their wettability difference.

The differences of adsorption and desorption capacity between the three water-bearing states were quantitatively characterized by the coefficient of variation of Langmuir volume and Langmuir pressure at different water-bearing states. Figure 10 shows the coefficients of variation of the ZJM sample were generally higher than those of the SH sample, indicating the ZJM sample was more susceptible to water with strong wettability.

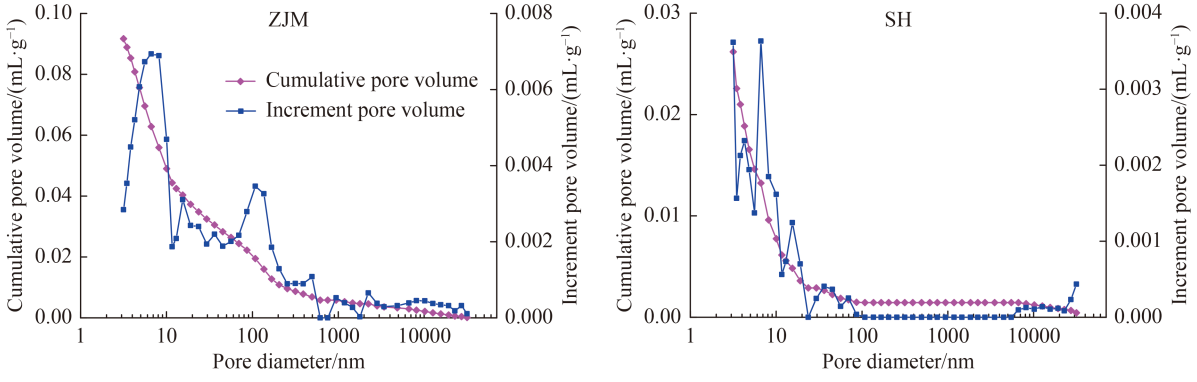

Fig. 8 MIP pore size distribution of coal samples.

Table 6 Statistics of pore size distribution of coal samples

Sample	Parameter	Macropore	Mesopore	Transitional pore	Micropore	Total
ZJM	Pore volume/(cm^3·g^{-1})	0.0053	0.0142	0.0296	0.0427	0.0917
	Proportion/%	5.77	15.45	32.24	46.55	100.00
SH	Pore volume/(cm^3·g^{-1})	0.0014	0.0000	0.0063	0.0184	0.0262
	Proportion/%	5.52	0.00	24.10	70.38	100.00

Notes: Macropore, pore diameter > 1000 nm; Mesopore, 100~1000 nm; Transitional pore, 10~100 nm; Micropore, < 10 nm.

Table 7 Water content of coal samples for IADE in different states

Sample	Dry/%	Equilibrium water/%	Saturated water/%
ZJM	0	9.65	35.07
SH	0	6.99	28.79

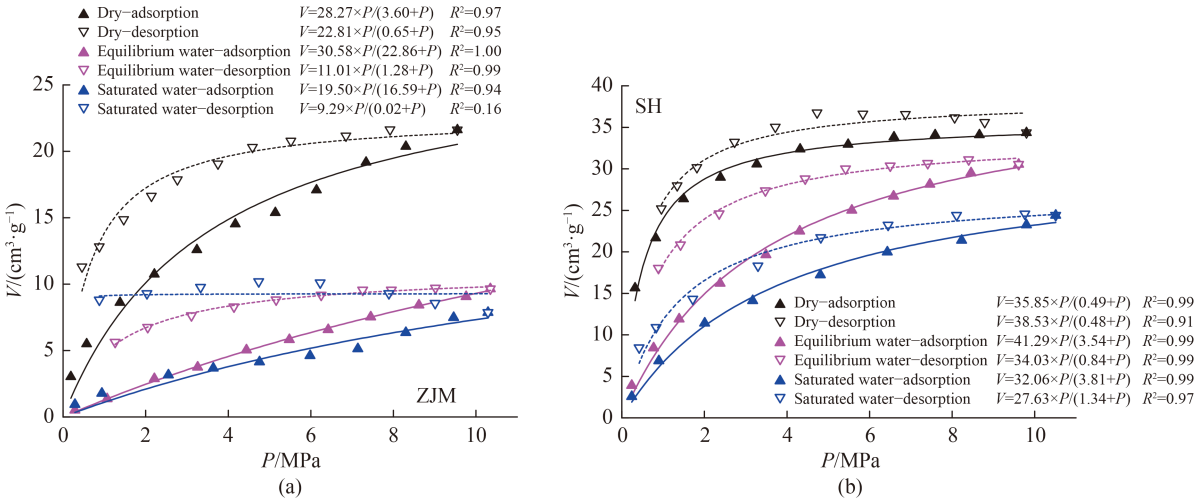

Fig. 9 Isothermal adsorption and desorption curves of coal samples.

4 Discussion

4.1 Quantitative characterization of desorption hysteresis

4.1.1 Desorption hysteresis constant

Quantitative characterization of desorption hysteresis is the basis for explaining the mechanism of this phenomenon. The change in Langmuir constant between adsorption and desorption is a direct indicator for desorption hysteresis. We define the following parameters:

$$V' = \frac{V_{LA} - V_{LD}}{V_{LA}} \times 100\%, \tag{2}$$

$$P' = \frac{P_{LA} - P_{LD}}{P_{LA}} \times 100\%, \tag{3}$$

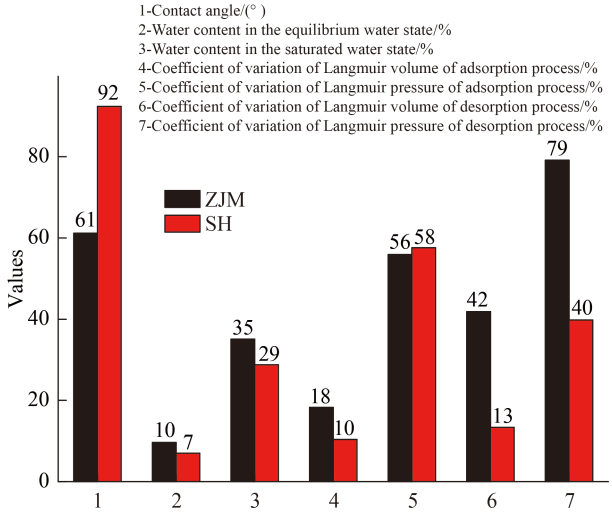

Fig. 10 Comparison of wettability and variation of adsorption/desorption constants of three water-bearing states between ZJM and SH samples.

where V' is the change-rate of the Langmuir volume between the adsorption process and desorption process, %; V_{LA} is the V_L of the adsorption process; V_{LD} is the V_L of the desorption process; P' is the change-rate of the Langmuir pressure between the adsorption process and desorption process, %; P_{LA} is the P_L of the adsorption process; and P_{LD} is the P_L of the desorption process. Both V' and P' tend to be positive because of desorption hysteresis. The slope of the desorption curve was smaller than that of the adsorption curve, which implied that both V_L and P_L of the desorption process were less than those of the adsorption process. V' and P' are called desorption hysteresis constants in this study; the larger their values, the more obvious the desorption hysteresis phenomenon. The calculated results are shown in Table 8.

The desorption hysteresis constant of the ZJM sample in all states was larger than that of the SH sample, indicating that the desorption hysteresis degree of low-rank coal was stronger than that of high-rank coal. In general, with the increase in water content, desorption hysteresis tended to be stronger, particularly for the ZJM sample. The desorption hysteresis of the SH sample in the dry state was not obvious, which was consistent with its homogenized pore structure. The value of P' was larger than that of V' as P' was more obviously affected by the slope of the adsorption/desorption curve, which was a better parameter to characterize desorption hysteresis.

Table 8 Calculation results of desorption hysteresis constant

Sample	State	V'/%	P'/%
ZJM	Dry	19.31	81.94
	Equilibrium water	64.00	94.40
	Saturated water	52.36	99.88
SH	Dry	−7.48	2.04
	Equilibrium water	17.58	76.27
	Saturated water	13.82	64.83

4.1.2 Desorption hysteresis area coefficient

An area parameter based on the isothermal adsorption and desorption curves was further introduced to quantitatively characterize the desorption hysteresis. The desorption hysteresis area coefficient *HI* is defined as follows:

$$HI = A_m/A_t, \quad (4)$$

where A_m is the measured hysteresis area and A_t is the hysteresis area under theoretical, completely irreversible conditions, as shown in Fig. 11. *HI* is between 0 and 1, the closer to 1, the stronger the desorption hysteresis. *HI* is 0 when the desorption and adsorption curves completely coincide, representing a completely reversible desorption state. *HI* is 1 when the desorption curve is a horizontal line parallel to the *x*-axis, meaning that the desorption was completely irreversible, and there was no decrease in adsorption volume during the pressure-reduction process.

The *HI* was calculated for each coal sample at different water-bearing states to quantitatively characterize the degree of desorption hysteresis (Table 9). Curve integration was applied to calculate area using Origin Pro 2018. The results of the calculation showed that the *HI* of the ZJM sample tended to increase gradually with an increase in water content and nearly approached a completely irreversible state in the saturated water state (*HI* = 0.99). The difference in the *HI* of the SH sample between all three water-bearing states was relatively small, and the equilibrium-water state had the highest *HI*. Water will aggravate the degree of desorption hysteresis, particularly in low-rank coal, because of the strong wettability and complex pore-throat structure. The *HI* of the ZJM sample was higher than that of the SH sample for each water state, which was consistent with the desorption hysteresis constant results, reflecting that the desorption hysteresis of low-rank coal was stronger than that of high-rank coal (Table 9). Since *HI* represents the overall characteristics of the isothermal adsorption and desorption curves, it is a better parameter in characterizing desorption hysteresis compared to desorption hysteresis constant.

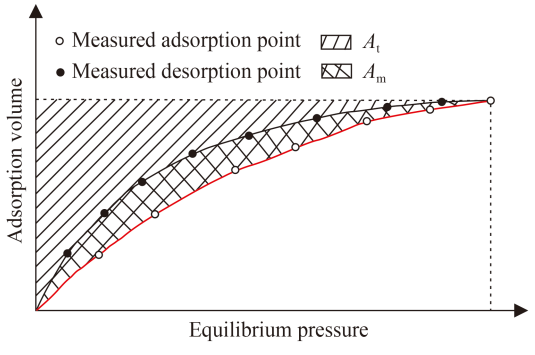

Fig. 11 Schematic for quantitative calculation of desorption hysteresis (Wang et al., 2016).

4.2 Desorption hysteresis mechanism

The desorption hysteresis of coal has been widely investigated (Zhang and Liu, 2017; Zhou et al., 2020), and it originates from the limited desorption and diffusion caused by pore deformation after adsorption (Wang et al., 2016). This is explained from the perspective of coal–gas interaction, yet the question of whether there are new control factors of desorption hysteresis under coal–water–gas three-phase coupling remains. From the experimental results of this study, water will intensify the degree of desorption hysteresis. The blocking effect of water on adsorption pore results in a relatively closed pressure system, and the gas cannot be effectively desorbed. Low-rank coal has strong wettability, and the water in macropores limits the pressure drop in mesopores and micropores, affording stronger desorption hysteresis. High-rank coal has poor wettability with mesopores and micropores dominating, and the negative influence of water on methane desorption is relatively weak. The solution phase of gas could be another factor enhancing desorption hysteresis under the condition of coal–water–gas coexistence (Zhou et al., 2020).

In general, the limited spread of pressure drop caused by the nonuniform distribution of pores at various pore-size levels intensify the desorption hysteresis of low-rank coal. In addition, the strong wettability of low-rank coal will increase the amount of dissolved gas in the water-bearing state, which may further enhance desorption hysteresis.

4.3 Adsorption and desorption mode

Based on the aforementioned analysis, the following adsorption and desorption mode under the coal–water–gas three-phase coupling system of high- and low-rank coal samples is formed (Fig. 12): the pore size of the low-rank coal sample is obviously larger than that of the high-rank coal sample, and water easily enters the pores under strong wettability, which reduces the adsorption potential of methane. This negative influence is exerted in the equilibrium-water stage and is further strengthened in the saturated-water state.

For the dry state of low-rank coal sample, methane

Table 9 Calculation results of desorption hysteresis area coefficient *HI*

Sample	State	A_m	A_t	*HI*
ZJM	Dry	37.32	56.90	0.66
	Equilibrium water	24.19	34.62	0.70
	Saturated water	42.93	43.19	0.99
SH	Dry	22.66	43.12	0.53
	Equilibrium water	44.16	71.78	0.62
	Saturated water	33.68	72.75	0.46

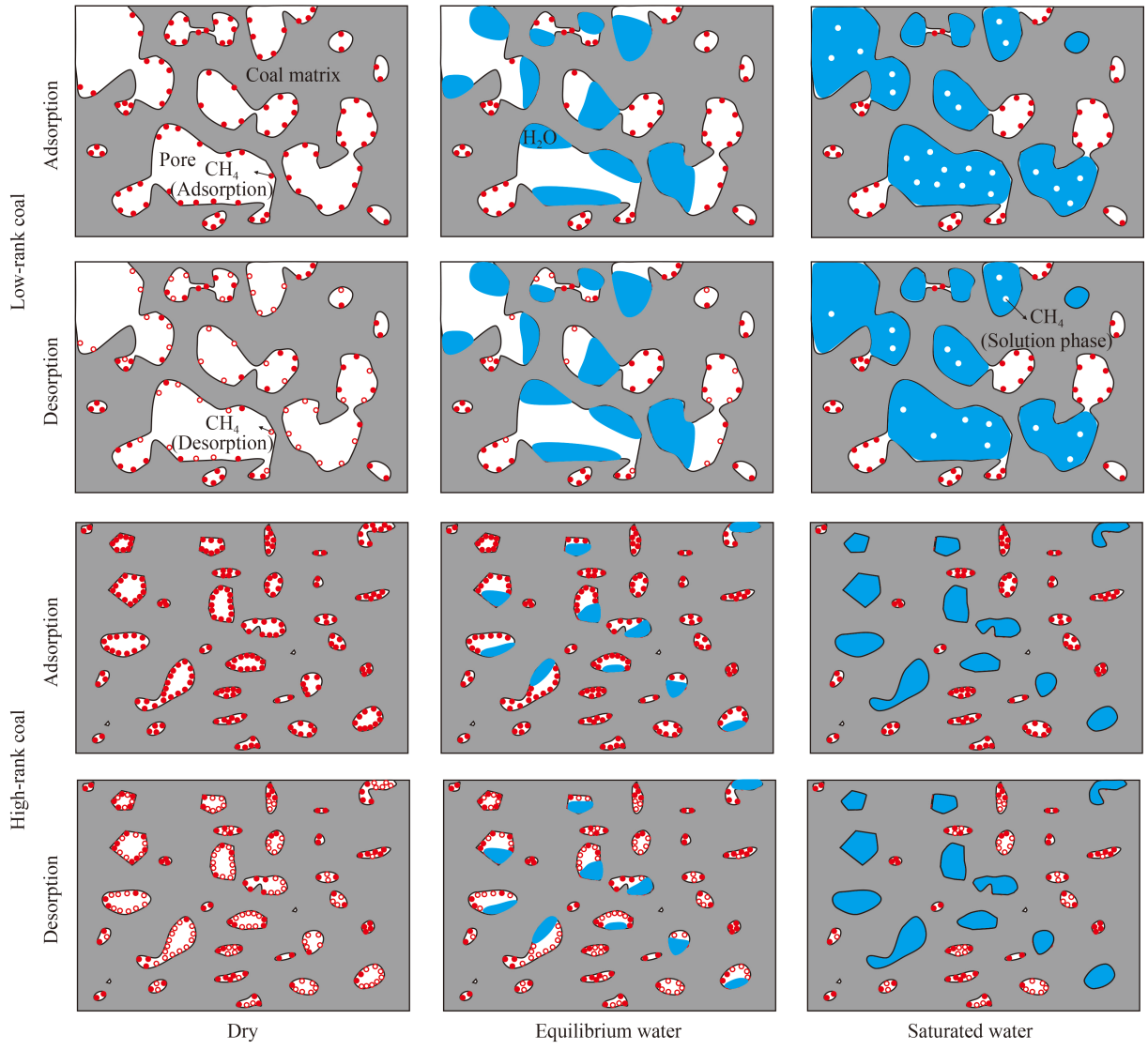

Fig. 12 Three-phase coupled adsorption–desorption mode for low- and high-rank coals.

adsorbed in large pores preferentially desorbs, and desorption hysteresis occurs because of the pore deformation after adsorption and limited pressure spreading in complex pore-and-throat structures with nonuniform pore-size distribution; in the equilibrium-water state, the large pores are preferentially filled with water. Methane adsorption volume reduces because of the occupation of adsorption sites by water. Particularly, the ratio of available sorption sites for desorption relative to adsorption decreases, resulting in a considerable desorption hysteresis phenomenon; in the saturated water state, methane adsorption capacity is further reduced. Methane is mainly absorbed in small pores, whereas large pores are filled with water, which may contain a certain amount of dissolved gas. The ratio of available sorption sites for desorption relative to adsorption further decreases. The dual effect of saturated water and dissolved gas leads to a considerable desorption hysteresis.

The high-rank coal sample is characterized by a uniform pore size distribution. The adsorption capacity decreases in the order of dry state, equilibrium-water state, and saturated-water state because of the reduction of adsorption sites. However, the impact of water on the adsorption of the high-rank coal sample is weaker than that of the low-rank coal sample due to weak wettability. In the equilibrium-water state, water preferentially fills large pores and occupies the adsorption sites that easily desorb methane, which increases the relative proportion of methane that is difficult to desorb and enhances desorption hysteresis during the desorption process; in the saturated-water state, more water enters into the smaller pores and reduces the methane adsorption and desorption capacity therein. However, the influence of water on the desorption hysteresis of the high-rank coal sample is more complex than that of the low-rank coal sample. There is no clear trend of desorption hysteresis with the increase in water content. The intensity of desorption hysteresis caused by water intrusion is limited by a low

proportion of macropores and uniform pore size distribution, and the difference in desorption hysteresis between the dry, equilibrium-water, and saturated-water states is relatively small.

5 Conclusions

1) The ZJM sample had stronger water wettability than that of the SH sample. The NIE process of the ZJM sample exhibited the characteristics of a rapid imbibition rate and high total imbibition volume, whereas the SH sample showed the characteristics of a slow imbibition rate, low total imbibition volume, and pore increments dominated by mesopores and micropores. The relatively large pore size of low-rank coal provides favorable conditions for the rapid imbibition of water into the sample.

2) ZJM sample had a higher porosity and permeability than the SH sample, which constituted the structural basis for its strong wettability. The MIP showed that the ZJM sample had a high pore volume (0.0917 cm^3/g), large pore size (8.96 nm on average), and low MWE (59.60%), reflecting a diverse pore-size combination; SH sample had a low pore volume (0.0262 cm^3/g), small pore size (5.77 nm on average), and high MWE (97.62%), which indicates the homogenization of its pore-throat system.

3) Water reduced the adsorption capacity of coal toward methane, and hindered efficient desorption, which was reflected more considerably in ZJM sample. The desorption hysteresis of the ZJM sample was stronger than that of the SH sample and was more susceptible to water. The adsorption–desorption mode of high- and low-rank coal samples under coal–water–gas three-phase coupling was constructed, which deepened the understanding of the differences in the formation and development mechanisms between the two types of CBM reservoirs.

Acknowledgments This work was supported by the National Natural Science Foundation of China (Grant No. 42002195); Shaanxi Province Natural Science Foundation of China (No. 2019JQ-192); Special Research Project of Natural Science of Education Department of Shaanxi Province (No. 20JK0752); China Postdoctoral Science Foundation (No. 2018M631181); Foundation Research Project of Shaanxi Provincial Key Laboratory of Geological Support for Coal Green Exploitation (No. MTy2019-08); Open Fund of Key Laboratory of Coalbed Methane Resources and Reservoir Formation Process of the Ministry of Education (China University of Mining and Technology) (No. 2020-002); Major Science and Technology Project of Inner Mongolia Autonomous Region (2021ZD0034-3); and Outstanding Youth Science Fund of Xi'an University of Science and Technology (2021-14). We thank all of the parties that contributed to this publication.

References

Abdulelah H, Negash B M, Al-Shami T M, Abdulkareem F A, Padmanabhan E, Al-Yaseri A (2021). Mechanism of CH_4 sorption onto a shale surface in the presence of cationic surfactant. Energ Fuel, 35(9): 7943–7955

Alvarez J O, Schechter D S (2016). Application of wettability alteration in the exploitation of unconventional liquid resources. Pet Explor Dev, 43(5): 832–840

Arkhipov V A, Paleev D Y, Patrakov Y F, Usanina A S (2014). Coal dust wettability estimation. J Min Sci, 50(3): 587–594

Askalany A A, Saha B B (2017). Towards an accurate estimation of the isosteric heat of adsorption—— a correlation with the potential theory. J Colloid Interface Sci, 490: 59–63

Azizian S, Bashiri H (2008). Description of desorption kinetics at the solid/solution interface based on the statistical rate theory. Langmuir, 24(22): 13013–13018

Chen Y, Fu H Y, Ma D M, Duan Z H, Zhang Y P, Yang F, Li W B, Zheng C, Teng J X (2021). Differences of the pore structure and methane adsorption/desorption between vitrain and durain of low-rank coals: case study in the Huanglong Coalfield, southern Ordos Basin, China. J Energy Eng, 147(5): 04021038

Clarkson C R, Bustin R M (2000). Binary gas adsorption & desorption isotherms: effect of moisture and coal composition upon carbon dioxide selectivity over methane. Int J Coal Geol, 42(4): 241–271

Filippova N L (1998). Adsorption and heat of adsorption onto polymer particular surface by inverse gas chromatography. J Colloid Interface Sci, 197(1): 170–176

Grinev I V, Zubkov V V, Samsonov V M (2016). Calculation of isosteric heats of molecular gas and vapor adsorption on graphite using density functional theory. Colloid J, 78(1): 37–39

Guo C, Qin Y, Ma D M, Lu L L (2020a). Pore structure response of sedimentary cycle in coal-bearing strata and implications for independent superposed coalbed methane systems. Energy Sources A Recovery Util Environ Effects: 1–20

Guo C, Qin Y, Ma D M, Xia Y C, Bao Y, Chen Y, Lu L L (2020b). Pore structure and permeability characterization of high-rank coal reservoirs: a case of the Bide-Santang Basin, western Guizhou, south China. Acta Geol Sin (English Edition), 94(2): 243–252

Guo C, Qin Y, Lu L L (2018). Terrestrial heat flow and geothermal field characteristics in the Bide-Santang Basin, western Guizhou, south China. Energy Explor Exploit, 36(5): 1114–1135

Guo C, Qin Y, Sun X Y, Wang S Q, Xia Y C, Ma D M, Bian H Y, Shi Q M, Chen Y, Bao Y, Lu L L (2021). Physical simulation and compatibility evaluation of multi-seam CBM co-production: implications for the development of stacked CBM systems. J Petrol Sci Eng, 204: 108702

Guo C, Qin Y, Xia Y C, Ma D M, Han D, Chen Y, Chen W, Jian K, Lu L L (2017). Geochemical characteristics of water produced from CBM wells and implications for commingling CBM production: a case study of the Bide-Santang Basin, western Guizhou. China. J Petrol Sci Eng, 159: 666–678

Guo C, Qin Y, Ma D M, Xia Y C, Chen Y, Si Q H, Lu L L (2021). Ionic composition, geological signature and environmental impacts of coalbed methane produced water in China. Energy Sources A Recovery Util Environ Effects, 43(10): 1259–1273

Hu Y, Zhang Q, Zhou G, Wang H, Bai Y, Liu Y (2021). Influence mechanism of surfactants on wettability of coal with different

metamorphic degrees based on infrared spectrum experiments. ACS Omega, 6(34): 22248–22258

Ji H J, Peng X Q, Yao J, Mao Y N, Hou Y, Sheng Z K (2021). Insight into the influence of small organic molecules on the wettability of coal. Fuel, 294: 120537

Jia Z J, Ning Z F, Gao X W, Wang Q, Zhang W T, Cheng Z L (2021). Experimental investigation on molecular-scale mechanism of wettability alteration induced by supercritical carbon dioxide-water-rock reaction. J Petrol Sci Eng, 205: 108798

Jin Y, Li X, Zhao M Y, Liu X H, Li H (2017). A mathematical model of fluid flow in tight porous media based on fractal assumptions. Inter J Heat Mass Transfer, 108(Part A): 1078–1088

Li J Y, Li K Q (2016). Influence factors of coal surface wettability. J China Coal Soc, 41(S2): 448–453 (in Chinese)

Li Y, Yang J H, Pan Z J, Tong W S (2020). Nanoscale pore structure and mechanical property analysis of coal: an insight combining AFM and SEM images. Fuel, 260: 116352

Li Y, Zhang C, Tang D Z, Gan Q, Niu X L, Wang K, Shen R Y (2017). Coal pore size distributions controlled by the coalification process: an experimental study of coals from the Junggar, Ordos and Qinshui Basins in China. Fuel, 206: 352–363

Ma D M, Wang C T, Yang F, He Q, Li Q, Dai N, Zhang C Y, Suo G X (2018). Mass transfer process of desorption of CBM in Dafosi coal reservoir. J China Coal Soc, 43(S1): 219–228 (in Chinese)

Madani S H, Sedghi S, Biggs M J, Pendleton P (2015). Analysis of adsorbate-adsorbate and adsorbate-adsorbent interactions to decode isosteric heats of gas adsorption. Chem Phys Chem, 16(18): 3797–3805

Mohamed T, Mehana M (2020). CoalBed methane characterization and modeling: review and outlook. Energy Sources A Recovery Util Environ Effects: 1–23

Mohanty D, Chattaraj S, Singh A K (2018). Influence of coal composition and maturity on methane storage capacity of coals of Raniganj Coalfield, India. Int J Coal Geol, 196: 1–18

Oparin V N, Kiryaeva T A, Gavrilov V Y, Shutilov R A, Kovchavtsev A P, Tanaino A S, Efimov V P, Astrakhantsev I E, Grenev I V (2014). Interaction of geomechanical and physicochemical processes in Kuzbass coal. J Min Sci, 50(2): 191–214

Qin Y, Moore T A, Shen J, Yang Z, Shen Y, Wang G (2018). Resources and geology of coalbed methane in China: a review. Int Geol Rev, 60(5–6): 777–812

Qin Y, Song Q Y, Fu X H (2005). Discussion on reliability for co-mining the coalbed gas and normal petroleum and natural gas: absorptive effect of deep coal reservoir under condition of balanced water. Nat Gas Geosci, 16(4): 492–498 (in Chinese)

Salmachi A, Rajabi M, Wainman C, Mackie S, McCabe P, Camac B, Clarkson C (2021). History, geology, *in situ* stress pattern, gas content and permeability of coal seam gas basins in Australia: a review. Energies, 14(9): 2651

Sang S X, Zhu Y M, Zhang J, Zhang X D, Zhang S Y (2005). Experimental study on the influence of liquid water on methane adsorption by coal: an example from the southern Qinshui Basin coal reservoir. Sci Bull (Beijing), 50(S1): 70–75 (in Chinese)

Savitskyi D P (2015). Impact of the pH on angles of contact of water wettability of brown coal. J Water Chem Technol, 37(4): 155–160

Sharma A, Saikia B K, Phukan S, Baruah B P (2016). Petrographical and thermo-chemical Investigation of some North East Indian high sulphur coals. J Geol Soc India, 88(5): 609–619

Shen J, Qin Y, Fu X H, Wang G, Chen R, Zhao L J (2015). Study of high-pressure sorption of methane on Chinese coals of different rank. Arab J Geosci, 8(6): 3451–3460

Sun X X, Yao Y B, Liu D M, Zhou Y F (2018). Investigations of CO_2-water wettability of coal: NMR relaxation method. Int J Coal Geol, 188: 38–50

Varma A K, Khatun M, Mendhe V A, Hazra B, Singh B D, Dayal A M (2015a). Petrographic characterization and langmuir volume of shales from Raniganj Coal Basin, India. J Geol Soc India, 86(3): 283–294

Varma A K, Biswal S, Hazra B, Mendhe V A, Misra S, Samad S K, Singh B D, Dayal A M, Mani D (2015b). Petrographic characteristics and methane sorption dynamics of coal and shaly-coal samples from Ib Valley Basin, Odisha, India. Int J Coal Geol, 141−142: 51–62

Wang G D, Ren T X, Qi Q X, Wang K, Zhang L (2016). Mechanism of adsorption-desorption hysteresis and its influence on deep CBM recovery. J China Coal Soc, 41(1): 49–56 (in Chinese)

Wang Z W, Liu S M, Qin Y (2021). Coal wettability in coalbed methane production: a critical review. Fuel, 303: 121277

Xu W K, Li J H, Wu X, Liu D, Wang Z S (2021). Desorption hysteresis of coalbed methane and its controlling factors: a brief review. Front Earth Sci, 15(2): 224–236

Yao Y B, Liu D M (2012). Comparison of low-field NMR and mercury intrusion porosimetry in characterizing pore size distributions of coals. Fuel, 95: 152–158

Zhang R, Liu S M (2017). Experimental and theoretical characterization of methane and CO_2 sorption hysteresis in coals based on Langmuir desorption. Int J Coal Geol, 171: 49–60

Zhang S Q, Wu G G (2017). Coal Chemistry. Xuzhou: China University of Mining and Technology Press (in Chinese)

Zhou Y B, Zhang R L, Wang J, Huang J L, Li X R, Wu J G (2020). Desorption hysteresis of CO_2 and CH_4 in different coals with cyclic desorption experiments. CO_2 Util, 40: 101200